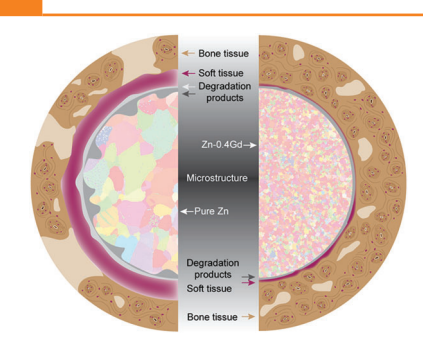


RESEARCH ARTICLES

H. Yang, B. Jia, X. Qu, K. Dai, Y. Zheng*.....2201184

Modified Biodegradation Behavior Induced Beneficial Microenvironments for Bone Regeneration by Low Addition of Gadolinium in Zinc



Trace amounts of gadolinium (Gd) are used here to modify the biodegradation behavior of zinc (Zn) via refinement of the intrinsic microstructure. As a result, the Zn-0.4Gd alloy implant generates beneficial microenvironments for bone regeneration by fulfilling the favorable biological role of Zn, contributing to improved osteogenesis and osseointegration.

www.advhealthmat.de

Modified Biodegradation Behavior Induced Beneficial Microenvironments for Bone Regeneration by Low Addition of Gadolinium in Zinc

Hongtao Yang, Bo Jia, Xinhua Qu, Kerong Dai, and Yufeng Zheng*

Zinc (Zn) shows a great potential as a biodegradable material for bone implants after a decade of systematic research and development. However, uncontrollable biodegradation behavior and biphasic dose-response prevent Zn from fulfilling its essential role in facilitating bone regeneration. In this study, the low addition of gadolinium (Gd) modifies the intrinsic microstructure of Zn in terms of grain size distribution, grain boundary misorientation, and texture. Adding Gd refines grain size distribution and creates a stronger basal plane texture in Zn, consequently, changing the current density distribution and reducing the anode dissolution rate during corrosion. As a result, uniform degradation is more predominant in Zn-0.4Gd alloy implant, in comparison to localized degradation in pure Zn implant in bone environments. The modified biodegradation behavior of the Zn-0.4Gd alloy implant induces significantly better new bone formation and osseointegration compared to the pure Zn implant. Therefore, Gd with trace amounts is able to tune the degradation behavior and improve the performance of Zn-based implants in promoting bone regeneration.

H. Yang, Y. Zheng School of Engineering Medicine Beihang University Beijing 100191, P. R. China E-mail: yfzheng@pku.edu.cn

H. Yang

School of Materials Science and Engineering

Peking University

Beijing 100871, P. R. China

B. Jia, X. Qu

Department of Bone and Joint Surgery

Department of Orthopedics

Renji Hospital

Shanghai Jiao Tong University School of Medicine

Shanghai 200001, P. R. China

K. Dai

Department of Orthopedics

Shanghai Key Laboratory of Orthopedic Implant

Shanghai Ninth People's Hospital

Shanghai Jiaotong University School of Medicine

Shanghai 200011, P. R. China



The ORCID identification number(s) for the author(s) of this article can be found under https://doi.org/10.1002/adhm.202201184

DOI: 10.1002/adhm.202201184

1. Introduction

Zinc is an indispensable trace element that is required for normal skeletal growth and bone hemostasis.^[1] Dietary zinc deficiency has been related to impaired bone growth and development in humans.[2] At the cellular level, zinc promotes the proliferation of osteoblast cells and increases the ALP activity and other osteogenic processes.[3] Meanwhile, zinc inhibits osteoclastogenesis in a dose-dependent manner.[4] The beneficial effect of zinc in bone regeneration promotes the rapid development of zinc as a promising candidate for biodegradable orthopedic implants.^[5] However, zinc seems to fail to fulfill the anticipation when it comes to its therapeutic function during biodegradation. In a rat calvarial criticalsized bone defect model, pure zinc membrane did not present superior performance compared to the pure titanium membrane

in terms of osteogenic capability.^[6] Porous zinc scaffold failed to outperform pure Titanium (Ti) counterpart in bone formation and ingrowth in a rabbit cranial defect model.^[7] A common finding reveals that the effects of zinc on bone cells are dosedependent.^[8] In other words, the beneficial effects of zinc on bone formation only occur over a narrow dose range, doses above the range inhibit osteogenic activity. Therefore, we hypothesize that the underlying reason for pure zinc implants failing to play a positive role in bone regeneration is attributed to their unpleasant biodegradation behavior, which releases excess zinc to surrounding cells and tissues.

Surface modification and alloying are two common methodologies to improve the cytocompatibility and histocompatibility of zinc. Coatings include zinc phosphate, ^[9] zinc oxide, ^[10] calcium phosphate, ^[7] and collagen ^[11] have been applied to ameliorate the proliferation and differentiation of mesenchymal stem cells and MC3T3-E1 cells by delaying the degradation of zinc. However, these coatings only work in cellular experiments and lack in vivo verifications. Meanwhile, coatings greatly prolong the time frame required for the full biodegradation of zinc. Alloying is more prevailing as it modifies the intrinsic performance of zinc in terms of mechanical property, degradation behavior, and biocompatibility. ^[5a,12] Elements with beneficial effects on bone metabolism have been selected with priority. Alloying with calcium, magnesium, and strontium promoted the osteogenic capability of zinc significantly, and outperformed



www.advancedsciencenews.com

www.advhealthmat.de



titanium implants.^[5g,h,13] Certain contents of them are required to promote osteogenesis, but the solubility of them in zinc is quite low. Adding too much of these nutrient elements will result in galvanic corrosion and embrittlement.

Rare earth elements (REE) have been of particular interest in alloying magnesium (Mg) alloys considering their unique chemical and physical properties to refine microstructure, reduce impurity and defects, and modify corrosion resistance.[14] Two REE Mg-based devices have commercialized successfully in 2013 (Magnezix Compression Screw, Syntellix AG, Germany) and 2016 (Magmaris Bioresorbable Scaffold, Biotronik, Germany), respectively. Both compositions are modified from Mg alloy WE43, which contains 4 wt.% Y, 3 wt.% non-Y REEs, and 0.4 wt.% Zr.[15] Apart from the WE series, gadolinium (Gd) was used to strengthen magnesium through the solid solution and aging effect, and it adjusts its corrosion resistance by scavenging impurities (Nickel (Ni), iron (Fe), or copper (Cu) and stabilizing the corrosion layer.[16] The biological role of Gd in bone metabolism is lacking in studies. The reported intraperitoneal median lethal dose (LD₅₀ dose) of GdCl₃ was 550 mg kg⁻¹ in mice.^[17] For implants, high-dose addition of Gd (10%) in magnesium led to fast disintegration of the material within 12 weeks.^[18] As a result, the bone remodeling was disturbed, and accumulation of Gd was detected in the spleen, lung, liver, kidney, brain, muscle, and heart. In contrast, minor addition of Gd (0.2%) in magnesium manifested a favorable corrosion behavior with good osteoconductivity and biocompatibility in a rat femur model.[16a]

In this study, low amounts of Gd (0.4 wt.%) were added to zinc considering its limited solubility and biosafety. We hypothesize that the minor addition of Gd would refine the microstructure of zinc, accordingly, improve the biodegradation behavior and optimize the biological effects of zinc for bone regeneration during the degradation of Zn-Gd alloy implant. To testify to the above assumption, a series of studies were conducted in terms of material microstructure and mechanical property, corrosion behaviors under electrochemical, immersion, and physiological conditions, cellular activities, and osteogenic capability.

2. Results

2.1. Microstructure

The influence of Gd on the microstructure of Zn is investigated systematically and presented in Figure 1. The characteristic peak of GdZn₁₂ was detected by X-ray diffraction (XRD) at 40.3° 2 θ degree, Electron backscatter diffraction(EBSD) phase map showed a uniform distribution of GdZn₁₂ phase (red) in the Zn matrix (blue). The addition of Gd significantly refined both the uniformity and grain size of Zn significantly (Figure 1B). Grain size decreased from 71.24 µm of pure Zn to 20.02 µm of Zn-0.4Gd alloy, and the distribution of grain diameter was more concentrated in Zn-0.4Gd alloy. The ratio of misorientation at the small angle decreased while the peak of misorientation at the large angle shifted from 67 to 31° in Zn-0.4Gd alloy compared to Zn. The grain orientations and texture are analyzed in Figure 1C. In the pole figure, Z0 refers to the extruded direction, and X0 and Y0 refer to the transverse direction. Both pure Zn and Zn-0.4Gd alloy exhibited texture with basal planes largely parallel to the extruded direction (ED). Zn-0.4Gd alloy presented a stronger basal plane texture compared to that of pure Zn. Additionally, the texture was featured by a ring around the transverse plane (X0-Y0) in (0001) pole figure while it changed into two peaks in Zn-0.4Gd alloy. GdZn₁₂ phase showed only one peak around ED in (001) pole figure. Further looking into the crystal structure and chemical composition (**Figure 2**), GdZn₁₂ was in a cubic structure and the interplanar distance of (101) plane was 0.45 nm, which was larger than the 0.21 nm of (10 $\bar{1}$ 0) plane in Zn. The crystal structure of GdZn₁₂ was further confirmed by the SAED pattern. The elemental analysis detected 7.1 atomic percentage of Gd in GdZn₁₂ phase.

2.2. Mechanical Property

The influence of Gd addition on the mechanical performance of Zn is evaluated in terms of tension and microhardness (Figure 3). Generally, adding minor amounts (0.4 wt.%) of Gd improved both the strength and ductility of Zn significantly. Zn-0.4Gd alloy achieved a favorable balance between strength (UTS 180.59 ± 4.07 , YS 101.50 ± 14.48), hardness (53.23 ± 1.18), and plasticity (Elongation to failure 30.23 ± 8.23). The fracture surface of as-extruded Zn and Zn-Gd alloy is presented in Figure 3C. Pure Zn displayed features typical of a brittle fracture including intragranular cracks, cleavage steps, and cleavage planes surrounded by tearing ridges. For comparison, Zn-Gd alloy exhibited large number of dimples distributed over the entire fracture surface, indicating a typical ductile fracture mode.

2.3. In Vitro Corrosion Behavior

To evaluate the in vitro corrosion behavior of Zn-Gd alloy, electrochemical measurements are conducted in SBF solution at 37°C. EIS is collected at open circuit potential and displayed in Nyquist plots and Bode plots (Figure 4A). Nyquist plots consisted of two capacitive semi-circles at high and low frequencies, respectively. The high-frequency arc was assigned to the charge transfer process and the double layer capacitance, whereas the low frequency was assigned to the formation of corrosion products and diffusion process. Equivalent circuits (a) and (b) are used here to fit the impedance spectra of Zn and Zn-0.4Gd alloy, respectively. In both circuits, constant phase elements (CPE) are used rather than capacitors to compensate for surface inhomogeneity. The R_s element describes the resistance of the SBF solution. R_{n1} and CPE₁ elements represent the charge transfer process and double-layer capacitance. Rp2 and CPE2 elements correspond to the resistance and capacitance of corrosion products. G element (Gerischer impedance) relates to the diffusion process and bulk chemical reaction. The fitted results of elements in equivalent circuits are listed in **Table 1**. In circuit (a), the diffusion process and charge transfer process occur simultaneously. As a result, the interface resistance includes both charge transfer and mass transfer processes. In circuit (b), the diffusion process occurs after the charge transfer process. Moreover, N relates to surface roughness. A lower N value indicates a rougher surface condition.

The real-time in situ corrosion current density distribution of samples after an hour of incubation in a cell culture medium

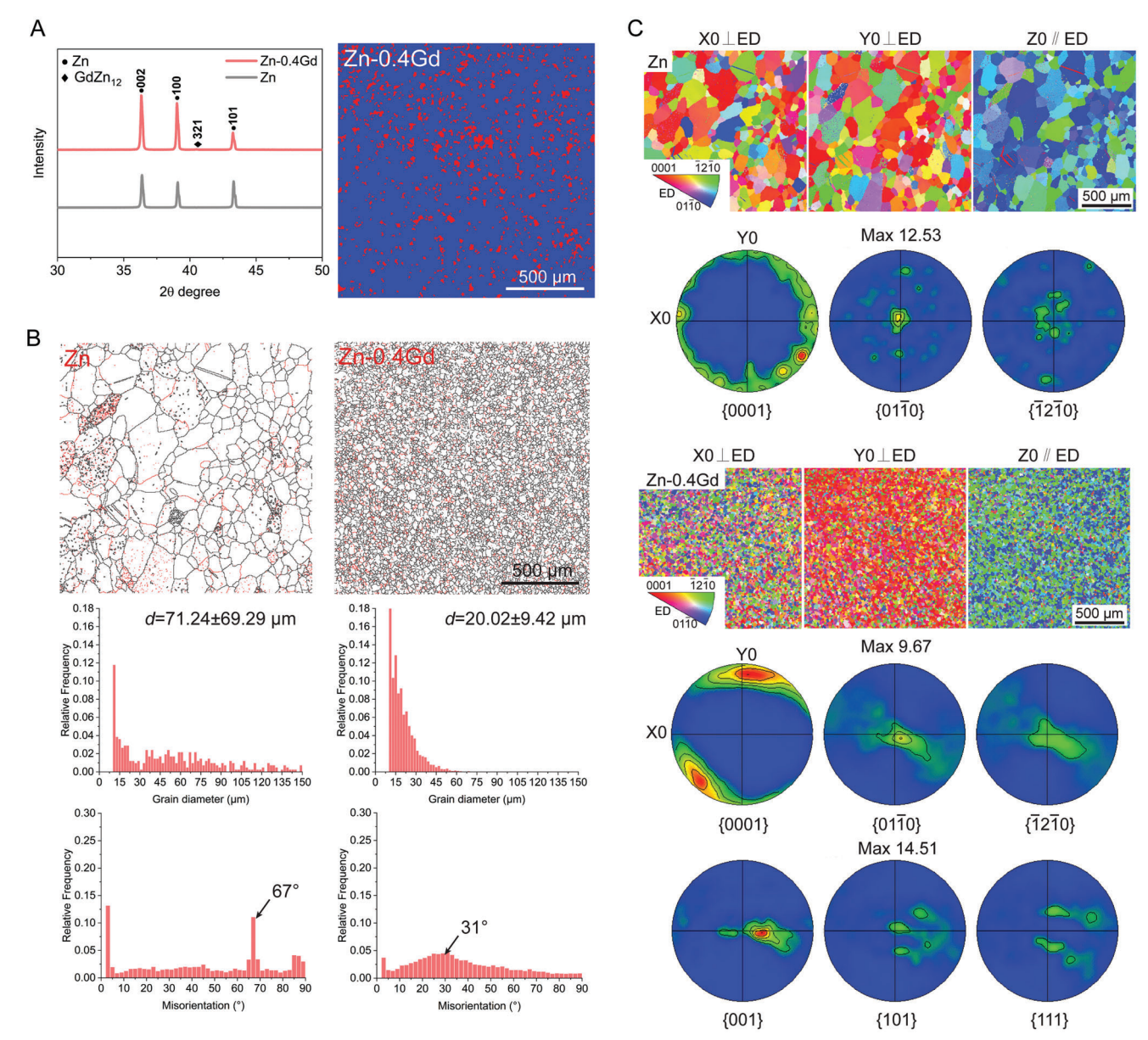


Figure 1. Microstructure of as-extruded Zn and Zn-0.4Gd alloy. A) XRD and phase map (red: GdZn12, blue: Zn). B) Grain boundary maps, quantitative analysis of grain diameter, and grain misorientation. Grains with orientations larger and lower than 15° are outlined in black and red, respectively. The calculated average grain size is displayed as *d*. C) EBSD pole figure (PF) orientation maps (ED: extrusion direction). For Zn-0.4Gd alloy, the first row of PF is Zn, and the second row is GdZn₁₂ phase.

is recorded by Scanning Vibrating Electrode Technique (SVET) (Figure 4B). Pure Zn caused a much larger anode current density than that of Zn-0.4Gd, which indicates a higher anode dissolution rate. In pure Zn, there was a critical anodic reaction zone with an anodic current density as high as 945 $\mu A~cm^{-2}$, while a larger cathodic reaction zone was adjacent to the anodic area. As a comparison, the current density distribution in Zn-0.4Gd alloy was much smoother, and the cathodic area was surrounded by a larger anodic reaction zone. The cathode/anode area ratio in pure Zn was higher than that of Zn-0.4Gd alloy. In general, the higher the cathode/anode area ratio, the deeper the corrosion penetration, and the high possibility of implant failure. Figure 4C

presents the corrosion morphology of samples after 1 week of immersion in a cell culture medium. Pure Zn showed a typical sign of intergranular corrosion with clear grain boundary corrosion. After adding small amounts of Gd, the grain boundary corrosion was replaced by a uniform corrosion mode.

2.4. In Vivo Degradation Behavior

A rat femur model was used here to investigate the in vivo degradation behavior of Zn-0.4Gd alloy implants, with pure Zn as a control. The X-ray images showed an excellent radiopacity of the

www.advhealthmat.de

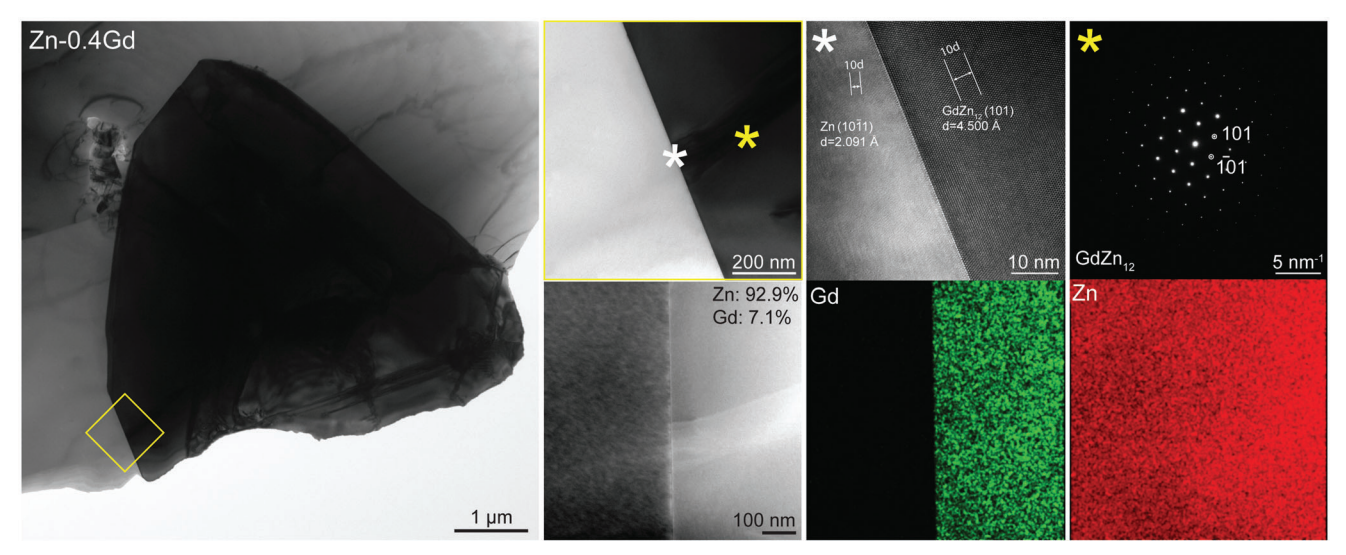


Figure 2. Bright-field (BF) TEM image, High-resolution (HR) TEM image, Selected area electron diffraction (SAED) pattern, and High-angle annular dark-field (HAADF) image with elemental mapping. The yellow rectangle and white asterisk show the magnification of the interface between the Zn and GdZn12 phases. The interplanar distance of the Zn and GdZn12 phases was measured by HRTEM. The yellow asterisk shows the area for the SAED pattern.

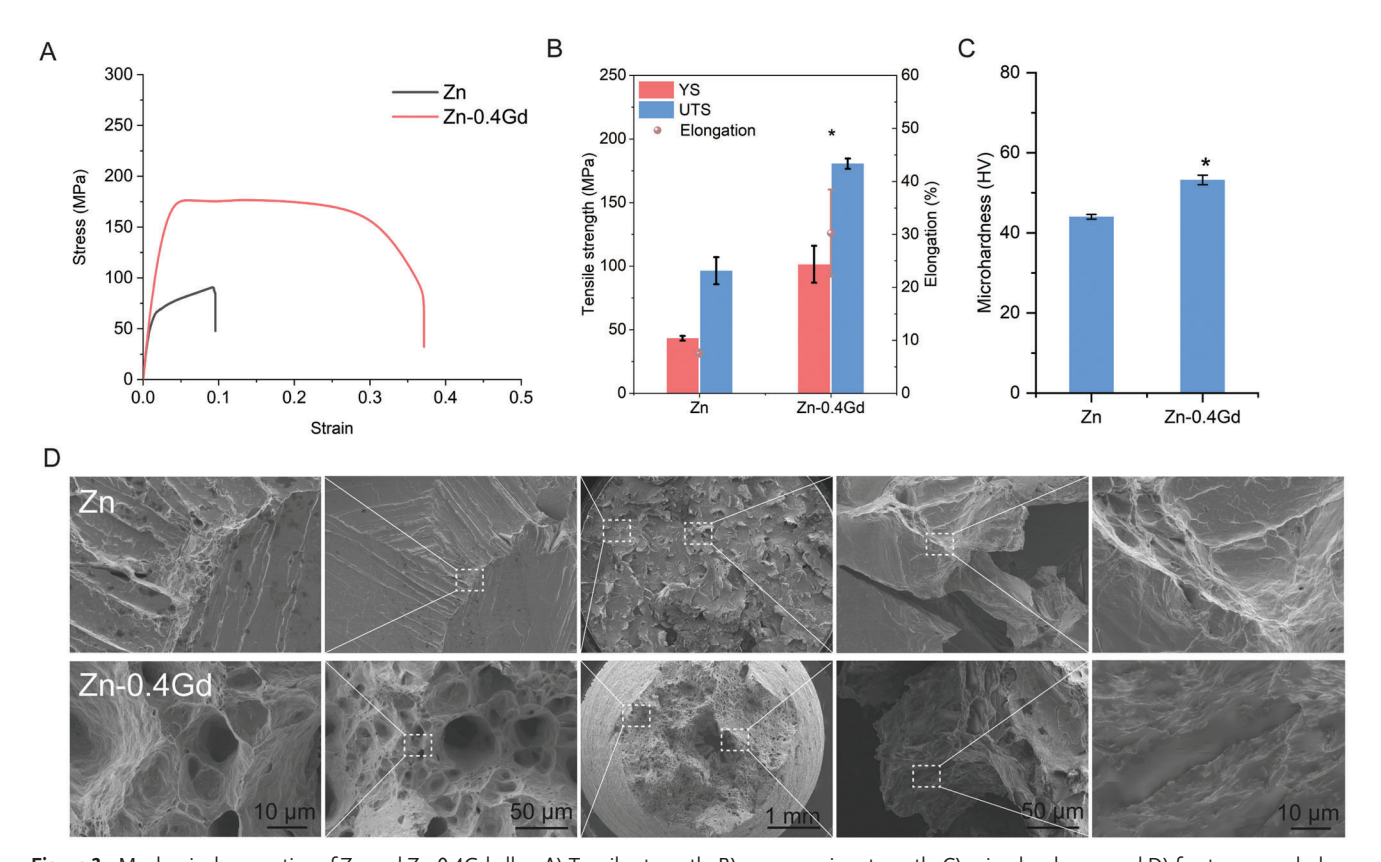


Figure 3. Mechanical properties of Zn and Zn-0.4Gd alloy. A) Tensile strength, B) compressive strength, C) microhardness, and D) fracture morphology after tension. Rectangles with white dashed lines indicate magnifications. Data presented as mean \pm standard deviation, n = 5, p-values are calculated using one-way ANOVA with Tukey's post hoc test, *p < 0.05 compared with Zn.



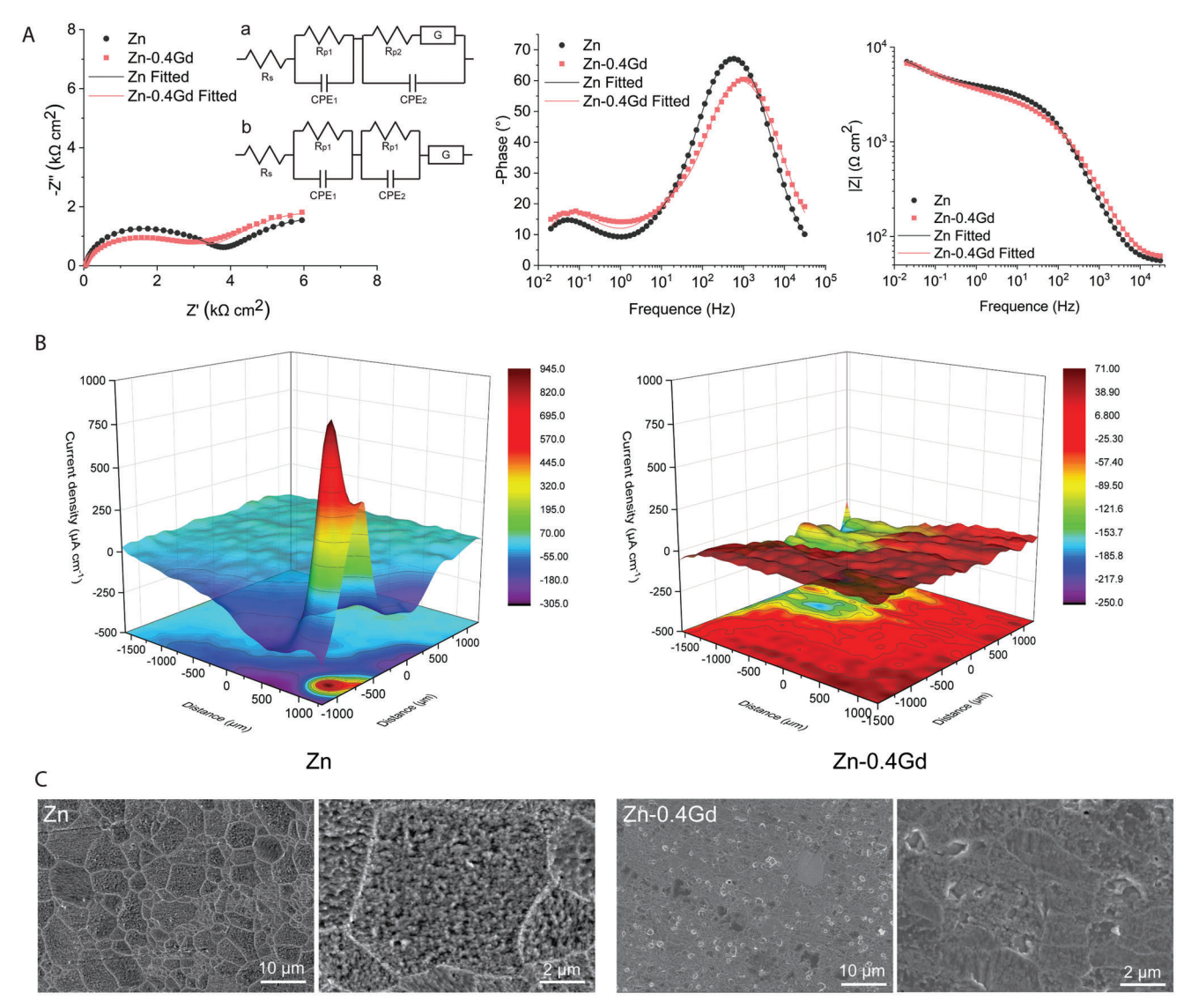


Figure 4. Corrosion behavior of pure Zn and Zn-0.4Gd alloy under in vitro conditions. A) Nyquist plots and Bode plots with equivalent circuits were used to fit the collected electrochemical impedance spectra (EIS). B) SVET monitoring of potential distribution on sample surface after immersion in cell culture medium (MEM) for 1 h . C) Corrosion morphologies (after cleaning) after immersion in MEM for a week.

Table 1. The fitted results of elements in equivalent circuits of EIS.

	Rs [Ω]	Rp1 [Ω]	Rp2 [Ω]	CPE1		CPE2		G		χ²
				Y0 $(\mu Mho \times s^N)$	N	Y0 (μ Mho \times s ^N)	N	Ka (s ⁻¹)	Y0 (μ Mho \times s ^(1/2))	
Zn	54.85 ± 1.91	1745 ± 445.48	1330 ± 282.84	1.52 ± 0.16	0.93	14.55 ± 1.34	0.84 ± 0.03	0.12	921 ± 352.14	0.03 ± 0.01
Zn-0.4Gd	50.28 ± 1.19	1560 ± 350.43	1957.5 ± 379.33	1.78 ± 0.21	0.88 ± 0.01	20.7 ± 5.07	0.75 ± 0.02	0.14 ± 0.05	612.75 ± 277.36	0.05 ± 0.01

Zn-based implants (**Figure 5**A). No osteolysis, deformation, dislocation, or gas shadow was found in the implantation sites. The adjacent cortical bone grew with a higher radiographic density over time, indicating the circumferential osteogenesis. Micro-CT reconstruction and quantitative measurements manifested limited degradation of both implants after 8 weeks. The volume loss

of both implants was <5%, resulting in degradation rates ranging from 0.11–0.14 mm per year. Detailed analysis of corrosion pits was conducted on the cross-sectional areas of implants at week 8 (Figure 5B). Distinct corrosion modes were observed in two groups in terms of pit size, pit depth, pit density, and penetration rate. For the pure Zn group, severe localized corrosion

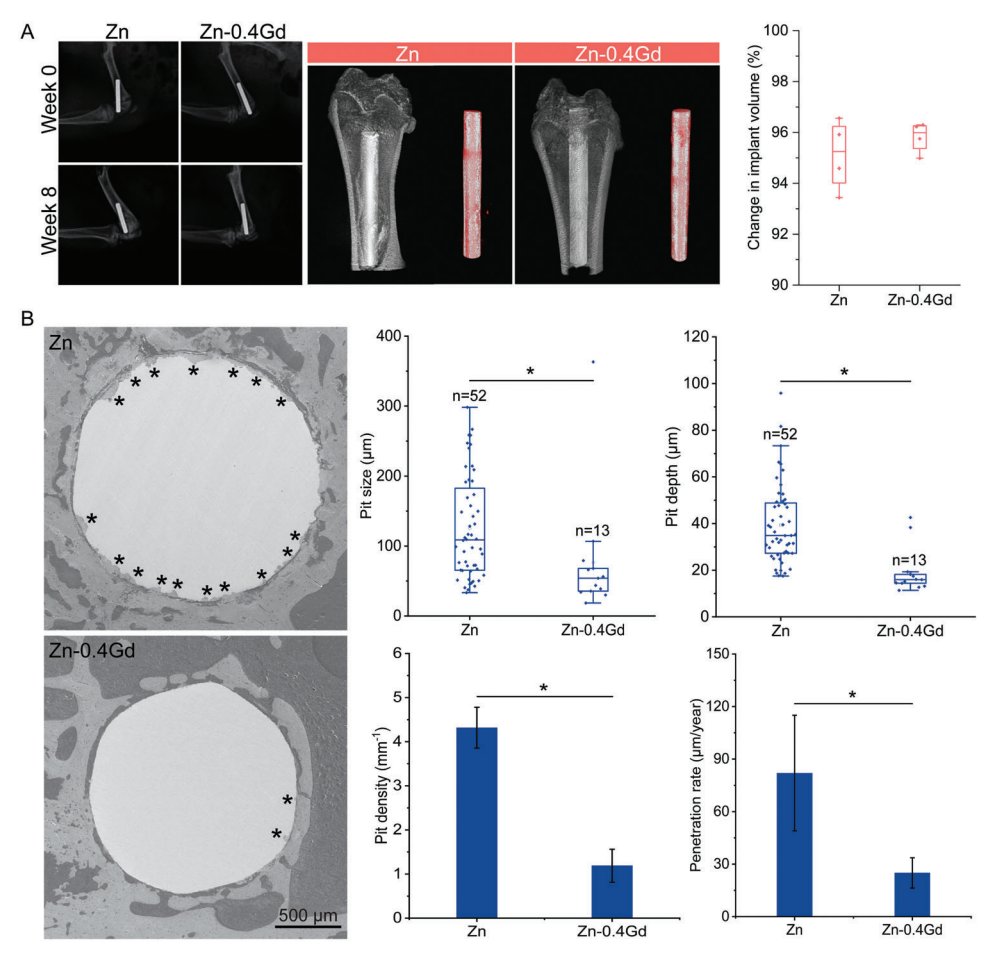


Figure 5. Degradation behavior of pure Zn and Zn-0.4Gd alloy implants in rat femurs. A) X-ray images post-surgery and at week 8, 3D reconstruction of implants with bone tissue at week 8, implants (silver) and degradation products (red) on the right, and quantitative analysis of implant volume and degradation rate (n = 4). B) Cross-sectional morphologies and quantitative analysis on pitting corrosion including pit size and pit depth (n = 52 for Zn group and n = 13 for Zn-0.4Gd group), pit density, and penetration rate (n = 3) of implants at week 8. Black asterisks indicate corrosion pits. For box whisker plots, box edges correspond to 25th and 75th percentiles, lines inside the box correspond to 50th percentiles, and whiskers include minimum and maximum of all data points. For bar plots, data presented as mean \pm standard deviation. *P*-values are calculated using one-way ANOVA with Tukey's post hoc test, *p < 0.05 compared with Zn.

happened around the edge of the implant. Pits with hundreds of microns in size and tens of microns in depth were typical in the Zn implant. In contrast, a more uniform mode with significantly fewer pits was found in the Zn-0.4Gd alloy implant. Quantitative measurement demonstrated that the pit size, pit depth, pit density, and penetration rate of the Zn-0.4Gd alloy implant were all significantly smaller than that of the pure Zn implant. The degradation behavior found in vivo corresponds well with the results of the electrochemical study.

2.5. Degradation Products

At the bone-implant interface, four components were discovered typically based on chemical compositions, and the evolution process of material degradation can be traced through their distribution (Figure 6). The common feature of both implants was that the zinc matrix (I) degraded into products II, followed by forming products III. Products II were composed of carbon, oxygen,

and zinc in a ratio of 3:4:3, which may be zinc oxide and zinc carbonate. Phosphorus and calcium appeared in products III in addition to carbon, oxygen, and zinc. New bone tissue (IV) was adjacent to products II or III. In Zn-0.4Gd alloy, the transition from degradation products (II and III) to new bone was continuous without the interference of fibrous tissue, indicating good osseointegration. In comparison, the localized corrosion in pure Zn resulted in the invasion of the fibrous layer and disrupted the direct contact between the implant and newly formed bone.

2.6. Cytocompatibility and Osteogenic Property

Preosteoblasts (MC3T3-E1) were used here to evaluate the cytocompatibility and osteogenic property of materials (**Figure** 7). Both materials showed toxicity on MC3T3-E1 cells when culturing with 100% extracts, while 50% extracts promoted cell proliferation. Cells adhered to the surface of pure Zn displayed a round and unhealthy morphology. In contrast, larger amounts



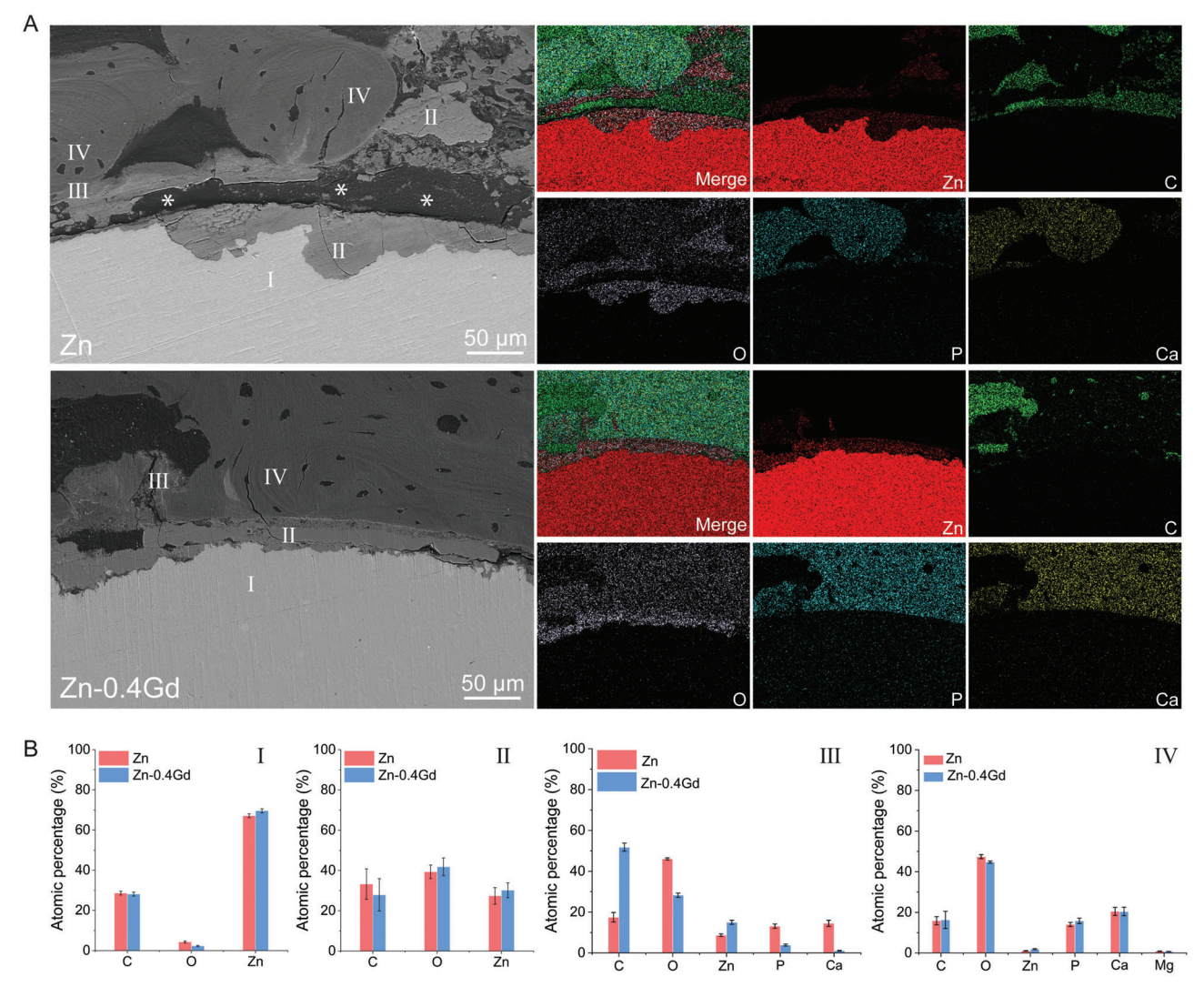


Figure 6. A) Cross-sectional examination of degradation morphology with corresponding elemental mappings, numbers I–IV indicates metallic implant (I), corrosion products (II-III), and new bone tissue (IV), respectively. Fibrous tissues are marked by white asterisks. B) Quantitative measurement of chemical compositions of regions I–IV in (A). Data presented as mean \pm standard deviation, n = 3.

of cells without spreading were found on the surface of the Zn-0.4Gd alloy. The Zn concentration in the two extracts had no significant difference, and Gd content was five orders of magnitude less than the Zn content. Therefore, the dose-dependent effect of Zn on osteogenesis was further studied by ALP activity and gene expression. 100%, 50%, and 25% extracts all showed significant inhibition on ALP activity while further dilution eliminated these effects. As for gene expression, 50% extracts inhibited the gene expression of Runx-2 whereas 25% extracts promoted the expression of OCN.

2.7. Histological Analysis

Van Gieson, Masson, and H&E staining are conducted respectively to investigate the osteogenesis, osseointegration, and inflammatory reactions of implant materials in **Figure 8**. Van Gieson staining showed that the new bone regeneration around

Zn-0.4Gd alloy was significantly better than pure Zn in terms of new bone volume and bone morphology. A ring of new bone tissue grew tightly around Zn-0.4Gd alloy while bone tissue distributed scattered and discontinuously around pure Zn. The bone-implant contact ratio in Zn-0.4Gd alloy was also much higher than pure zinc, implying better osseointegration, which is critical for the load transfer between implant and tissue. Moreover, the bone structure was more organized in the Zn-0.4Gd group. Compared to the pure zinc group, more red staining was found in the Zn-0.4Gd group, which might indicate a more mature state of bone tissue with more type II collagen. Additionally, mild inflammation was only found in the pure Zn group.

3. Discussion

The Zn-0.4Gd alloy implant outperformed the pure Zn implant significantly in terms of new bone formation and bone integration. In the bone-implant interface, less ingrowth of

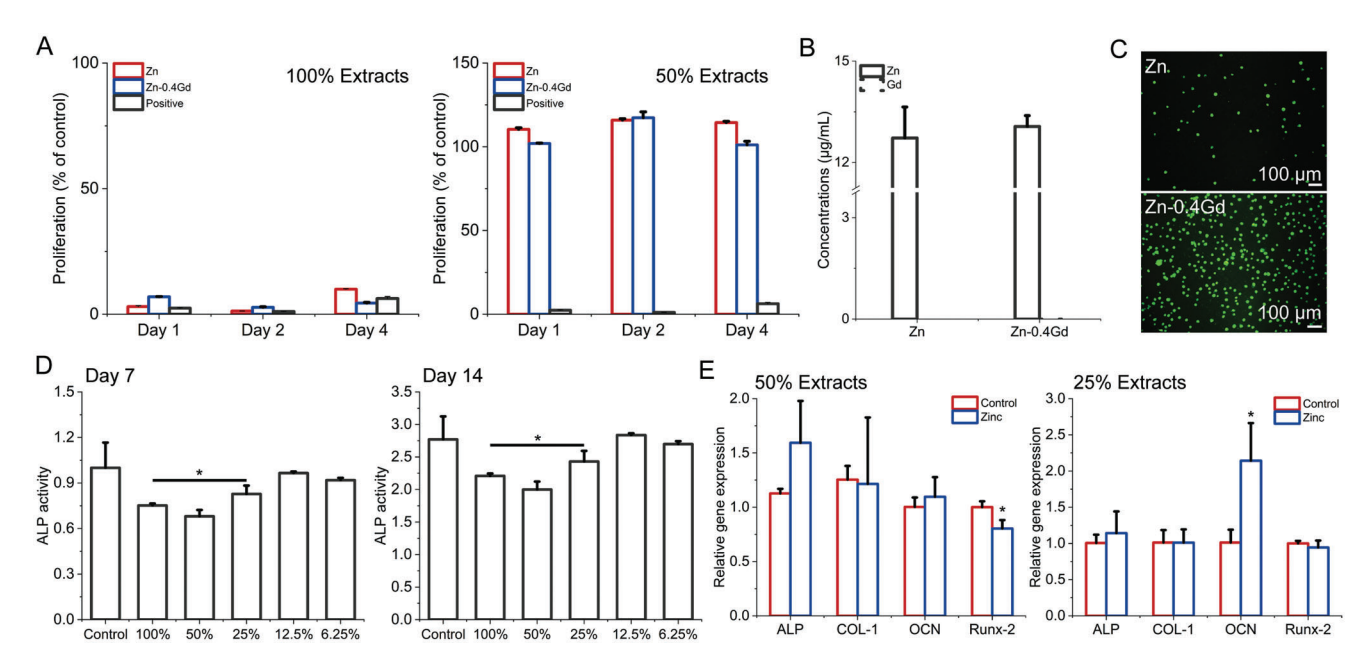


Figure 7. Cytocompatibility and osteogenic property of pure Zn and Zn-0.4Gd alloy on MC3T3-E1 cells. A) Cell viability with 100% and 50% extracts, B) Element concentrations of 100% extracts, C) Live/Dead staining of cells on the sample surface, D) ALP activity with gradient dilution of extracts, E) Gene expression of ALP, COL-1, OCN, and Runx-2 with 50% and 25% extracts. Data presented as mean \pm standard deviation. *P*-values are calculated using one-way ANOVA with Tukey's post hoc test, *p < 0.05.

fibrous tissue also indicates better biocompatibility of Zn-0.4Gd alloy implant. We hypothesize that adding trace amounts of Gd modifies the intrinsic microstructure of Zn, as a result, prompts its biodegradation behaviors with a more uniform feature, and finally fulfills the beneficial role of zinc in facilitating bone regeneration. **Figure 9** shows the detailed schematic diagram and the discussion will unfold from aspects of the effects of Gd on the biodegradation behavior and the modified microenvironments for bone regeneration.

3.1. The Effect of Gd on the Biodegradation Behavior of Zn

The addition of low amounts of Gd (0.4 wt.%) modified the microstructure of Zn in terms of grain size distribution and texture. The grain size decreases from 71.24 µm of pure Zn to 20.02 µm of Zn-0.4Gd alloy (Figure 1B). Meanwhile, the standard deviation of grain diameter reduces from 69.29 to 9.42 µm, indicating a more uniform grain size distribution. As a result, the strength, microhardness, and ductility of Zn-0.4Gd alloy are improved significantly (Figure 3) by the way of well-known Hall-Petch relations. Adding Gd creates a stronger basal plane texture compared to that of pure Zn. The alteration of intrinsic microstructure in Zn-0.4Gd alloy promotes directly the modification of its biodegradation behavior. Pure Zn implant undergoes a typically localized corrosion in the in vivo active environments while Zn-0.4Gd alloy implant experiences more uniform corrosion during implantation (Figure 5B). The real-time in situ monitoring reveals a significantly lower anode current density (up to 71 µA cm⁻²) in Zn-0.4Gd alloy than that of pure Zn (up to 945 µA cm⁻²), indicating a much smaller anodic dissolution rate (Figure 4). Moreover, the cathode/anode area ratio in Zn-0.4Gd alloy is smaller than that of pure Zn, which improves the corrosion homogeneity. The underlying reason behind the difference in electrochemical corrosion behavior attributes to the alteration of the material microstructure. First, the grain boundaries is a region, a few atomic diameters in thickness, over which a state of disorder exists where vulnerable to corrosion attack.^[19] Reduced grain size creates a higher grain boundary density. The larger volume fraction of grain boundaries combined with finer grain size ensures that pits formed are shallow and rather connected leading to the creation of uniform corrosion in Zn-0.4Gd alloy. On the contrary, the coarser-grained Zn with unevenly distributed grain boundaries contributed to intergranular corrosion, which leads to the formation of large localized pits. Second, texture plays a considerable role in the improvement of degradation behavior. In HCP crystal, basal planes are relatively more inert to corrosion than other planes.^[20] Consequently, Zn-0.4Gd alloy is least affected by intergranular corrosion considering its stronger basal texture. Although the second phase appears after adding Gd, the potential of GdZn₁₂ is close to Zn regarding Gd's low content, indicating a limited effect on galvanic corrosion. As a result, the Zn-0.4Gd implant shows a favorable uniform degradation mode in bone environments.

3.2. Modified Microenvironments in Zn-0.4Gd Alloy Implant for Bone Regeneration

Degradation of Zn in neutral body fluid produces zinc ions and hydroxyl groups in the surrounding local environments. [21] Precipitations include but are not limited to zinc oxide, zinc carbonate, zinc phosphate, and calcium-phosphorus complex when the local microenvironment becomes oversaturated. [22]

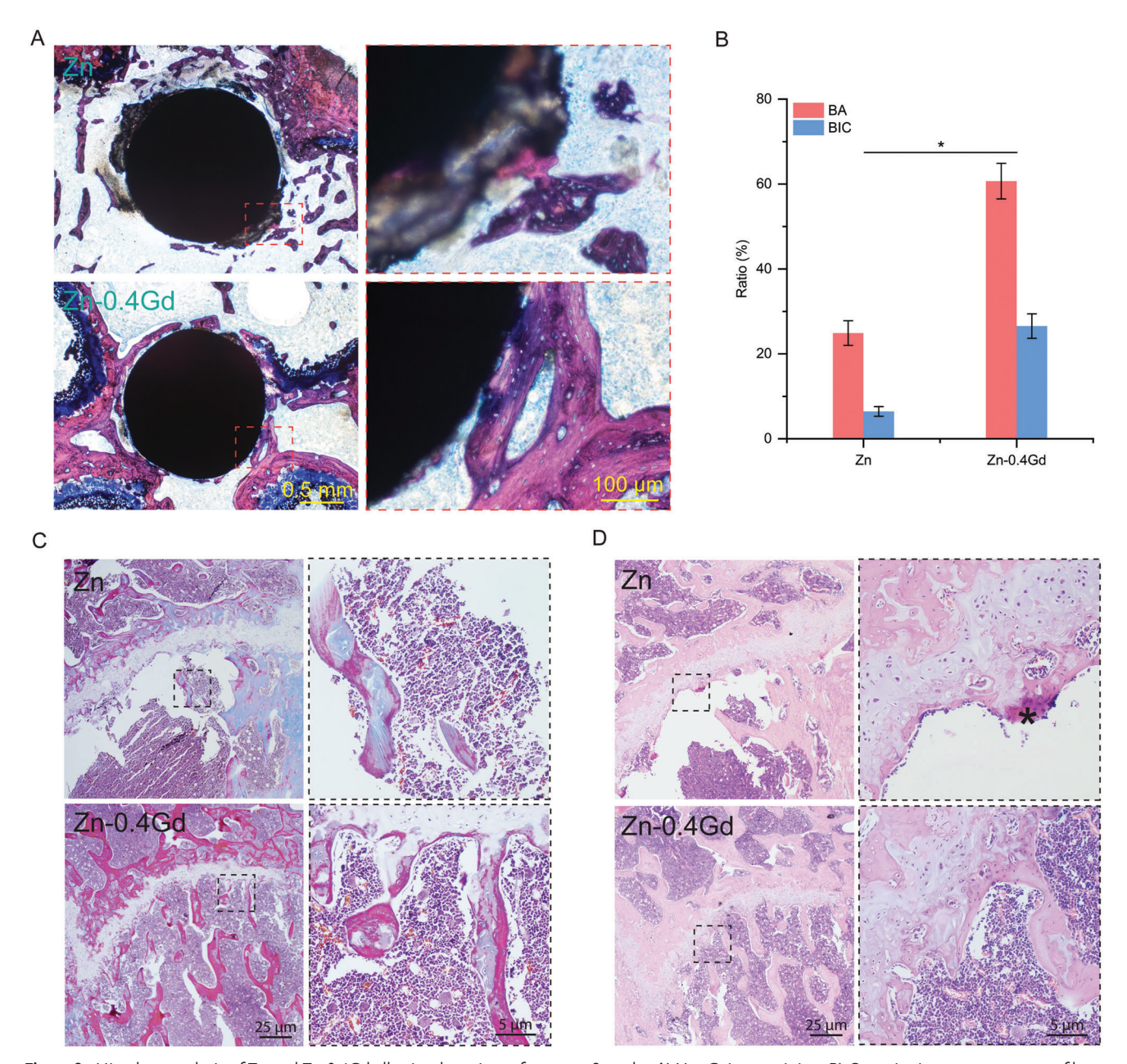


Figure 8. Histology analysis of Zn and Zn-0.4Gd alloy implants in rat femurs at 8 weeks. A) Van Geison staining, B) Quantitative measurements of bone area (BA) and bone-implant contact (BIC) ratio. C) Masson's trichrome staining and D) H&E staining, the black asterisk indicates inflammatory cells. Data presented as mean \pm standard deviation. Data presented as mean \pm standard deviation, n = 4, p-values are calculated using one-way ANOVA with Tukey's post hoc test, *p < 0.05 compared with Zn.

The major biological concern about zinc is rising from the dose-dependent effect of zinc ions on cells and tissues. Our cell experiments demonstrate that 100% extracts of both materials (zinc content $\approx 13~\mu g~mL^{-1}$) have cytotoxicity on preosteoblasts, but promoted proliferation is found with one-fold dilution (Figure 7). As for osteogenic differentiation, 50% extracts inhibited the gene expression of Runx-2 while 25% extracts enhanced the expression of OCN. Previous studies reported that zinc increased ALP activity of human osteoblast-like cells at a concentration $< 10 \times 10^{-6}$ M after 8 d of treatment, but decreased activity

at $50 \times 10^{-6}~\text{m}$. $^{[23]}$ The addition of zinc $(3.8\text{--}30 \times 10^{-6}~\text{m})$ to the cultured tibial resulted in a concentration-dependent increase in tibial DNA content and synthesis rate. $^{[24]}$ MC3T3-E1 cell proliferation was significantly enhanced with the peak at $50 \times 10^{-6}~\text{m}$ zinc while inhibited above $130 \times 10^{-6}~\text{m}$. $^{[3a]}$ Zinc increased the early phase of mineralization (14 days) in a dose-dependent manner ($1\text{--}20 \times 10^{-6}~\text{m}$) whereas the late phase of mineralization (21 days) was maximal at $1 \times 10^{-6}~\text{m}$. Therefore, zinc appears to promote bone formation and regeneration but within a limited dose range ($1\text{--}50 \times 10^{-6}~\text{m}$), such that too little or too much zinc



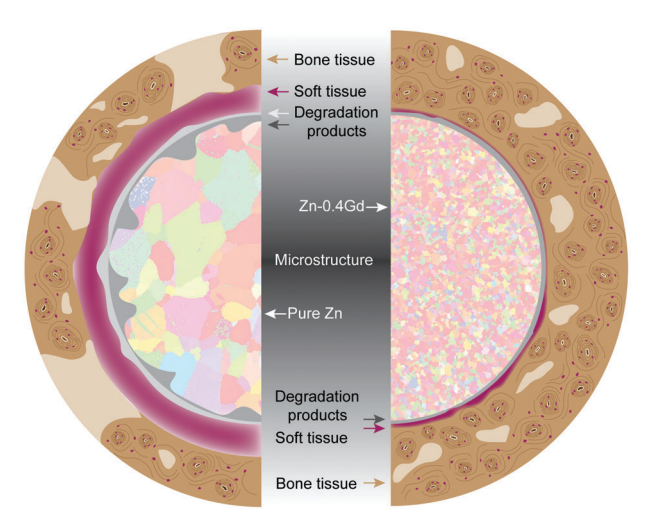


Figure 9. Schematic diagram illustrating the cross-section of pure Zn and Zn-0.4Gd alloy implants in bone environments.

is ineffective or even detrimental. Our in vivo study reveals that the Zn-0.4Gd alloy implant generates significantly better osteogenesis and osseointegration compared to that of the pure Zn implant. At the bone-implant interface, fibrous tissue invasion is observed around the localized corrosion sites in pure Zn, a "shielding off" the unfavorable area by bone tissue, which occupies the space for new bone and disrupts the direct bone-implant contact. In contrast, the transition zone between the Zn-0.4Gd alloy implant, degradation products, and new bone is continuous without the interference of the fibrous layer (Figures 6A and 7A). Therefore, it is reasonable to speculate that the biodegradation behavior of Zn-0.4Gd alloy generates more beneficial microenvironments in terms of zinc ion release for bone regeneration compared to that of pure Zn. Our previous studies revealed that Zn-Sr alloy promoted osteogenesis more significantly than both pure Zn and pure Ti. [5a,13b] This is attributed to the activation of the wnt/β-catenin, PI3K/Akt, and MAPK/Erk signaling pathways via the co-releasing of zinc and strontium during biodegradation. Strontium is a well-known element for its bioactive role in promoting bone formation and mineralization.^[26] Gd is a well-studied heavy rare earth element due to its wide applications as a radio imaging contrast agent. Previously studies have disclosed that the intraperitoneal median lethal dose (ID₅₀ dose) of GdCl₃ was 550 mg kg⁻¹ in mice while GdNO₃ induced acute toxicity at 300 mg kg⁻¹ in mice and 230 mg kg⁻¹ in rat.[17,27] Perinuclear vacuolization and cytoplasmic granularity in the parenchymal cells of the liver is observed in chronic oral exposure of large doses of the chloride, but otherwise few effects are found an impair liver function or other aspects of animal health.[17] The nephrotoxicity of Gd as a contrast agent is closely related to the specific complexing agent.^[28] Gd-induced NSF is overwhelmingly reported for the agent known as gadodiamide, with few reports for other agents.^[29] In bone environments, the biocompatibility of Gd containing implants is dose-dependent. High contents of Gd (10%) have been added into Mg, and results in rapid disintegration of the Mg-10Gd implant within 12 weeks. The fast releasing of degradation products interferes the normal bone remodeling and leads to accumulation of Gd in organs like spleen, lung, liver, kidney, brain, muscle, and heart.^[18] But minor addition of Gd (0.2%) modifies the degradation behaviors of Mg, and generates improved cytocompatibility in L929, MG63, and VSMC cells. The implants with low addition of Gd manifested an enhanced osteoconductivity after 2 months of implantation in a rat femur model. [16a] In a recently reported study, 0.1–0.3 wt.% Gd are introduced into Zn-1Mg alloy, which improves the cell viability of MG63 cells in 25% and 12.5% extracts. [30] Here, only 0.4 ng mL⁻¹ Gd element was detected in extracts of Zn-0.4Gd alloy, which is only one-thirty thousandth of the zinc element content. Therefore, the biodegradation and releasing behavior of zinc element should be the main reason for the histological difference induced by these two implants. The limited diffusion condition in the bone environment can easily generate local microenvironments with high zinc content when localized degradation happens, which may interfere with bone regeneration. On the contrary, uniform degradation with moderate zinc release is more likely to create beneficial microenvironments for bone regeneration. Recently, biodegradable metallic devices are proposed to enhance bone regeneration in distraction osteogenesis, and have been applied in the treatment of medial malleolar fractures with positive clinical outcomes.^[31] These studies may open up promising clinical translation examples for Zn-based biodegradable orthopedic implants.

4. Conclusion

This study explores the feasibility and effects of adding Gd in Zn for bone implant applications. Systematic characterizations from intrinsic material properties to extrinsic performances of implant lead to the following findings: i) Refined grain size distribution and stronger basal texture are observed after adding minor amounts of Gd. ii) Mechanical properties including tensile strength, ductility, and microhardness are significantly enhanced comprehensively through alloying with Gd. iii) The anode current density is reduced, and the current density distribution and cathode/anode area ratio are altered, resulting in a more uniform degradation mode of Zn-0.4Gd alloy in bone environments. iv) The modified biodegradation behavior of the Zn-0.4Gd alloy implant generates beneficial microenvironments for bone generation, contributing to better osteogenesis and osseointegration compared to that of the pure Zn implant.

5. Experimental Section

Material Preparation: Pure Zn and Zn-0.4Gd alloy were produced by Hunan Rare Earth Metal Material Research Institute. After casting, material ingots were homogenized at 350 °C for 48 h followed by water quenching. Then, ingots were hot extruded at 260 °C with an extrusion ratio of 36 and a rate of 1 mm s $^{-1}$. Thereafter, as-extruded pure Zn and Zn-0.4Gd alloy were cut into $\Phi 1.6 \times 15$ mm pins for implantation, and $\Phi 10 \times 1$ mm sample for the rest of the experiments. All samples were surface grounded to 2000 grit with SiC abrasive paper, followed by ultrasonically cleaning in ethanol and distilled water for minutes, respectively.

Microstructure Characterization: X-ray diffractometer (XRD, Rigaku DMAX 2400, Japan) using CuKa was operated at 40 kV and 100 mA to identify the phase composition of samples at a scan rate of 2° min⁻¹ and step of 0.02°. The sample surface perpendicular to the extrusion direction (ED) was polished by Ar⁺ ion polishing at 1 keV for 30 min in an ion thinning machine (Leica EM RES102). Grain size distribution, phase map,



www.advancedsciencenews.com





grain orientation, and texture were measured using Electron Backscattered Diffraction (EBSD, EDAX Velocity Super) in a SEM (JSM 7200F). Sample for Transmission Electron Microscope (TEM) was prepared by polishing to 60 μ m followed by electrolytic thinning using an electrolytic preparation equipment (TenuPol-5). Bright-field (BF) image, High-resolution (HR) image, Selected area electron diffraction (SAED) pattern, and High-angle annular dark-field (HAADF) image with elemental mapping were obtained by an FEI TEM (FEI Talos F200X).

Mechanical Tests: Tensile test samples were machined along the extrusion direction according to ASTM-E8-04a. Tensile test was conducted in a universal test machine (Instron 5969, USA) under room temperature at a displacement rate of $1\times 10^{-4}~{\rm s}^{-1}$. Yield strength was measured as the stress at which the 0.2% plastic deformation occurred. The fracture morphology was observed under a SEM (Hitachi S-4800, Japan). Microhardness was carried out in a tester (SHIMADZUHMV-2t) with 0.1 kN loading force and 15 s dwell time. An average of five measurements were taken for each group.

Corrosion Tests: The electrochemical tests were carried out using a three-electrode cell (counter electrode (Pt), saturated calomel electrode, and work electrode) in an electrochemical working station (Autolab, Metrohm, Switzerland) at 37 °C in Simulated Body Fluid solution (NaCl 8.035 g L⁻¹, KCl 0.25 g L⁻¹, K₂HPO₄·3H₂O 0.231 g L⁻¹, NaHCO₃ 0.355 g L⁻¹, HCl (36–38%) 39 mL L⁻¹, CaCl₂ 0.292 g L⁻¹, Na₂SO₄ 0.072 g L⁻¹, MgCl₂·6H₂O 0.311 g L⁻¹, Tris 6.118 g L⁻¹, pH 7.4). The open-circuit potential (OCP) was monitored for 5400 s. The Electrochemical Impedance Spectroscopy (EIS) measurement was conducted by applying 10 mV perturbation to OCP value in a frequency range from 105 to 10⁻² Hz. Equivalent circuits were created in a NOVA 2.1 software (Autolab, Metrohm, Switzerland). An average of five samples were taken for each group. The SVET measurement was carried out in alpha-minimum essential medium (MEM) at room temperature for 24 h at a 100 µm step size. The SVET system from Applicable Electronics Inc. (USA) was used. Immersion test was conducted in MEM medium at 37 °C for a week. Corrosion products were removed by CrO₃ solution and imaged by SEM.

Cell Experiments: Preosteoblasts (M3T3-E1, ATCC CRL-2594) were used here to evaluate the cytocompatibility and osteogenic property of pure Zn and Zn-0.4Gd alloy. Sample extracts (100%) were prepared by incubating samples in cell culture medium at a ratio of 1.25 mL cm $^{-2}$ followed by gradient dilution. Element concentration in the extract was measured by ICP-OES (iCAP6300, Thermo, USA). Cells were cultured with an $\alpha\text{-MEM}$ culture medium supplemented with 10% FBS, 1% penicillin (100 U mL $^{-1}$), and streptomycin sulfate (100 mg mL $^{-1}$) (Gibco, Grand Island, NY) in 37 °C, 5% CO $_2$, and saturated humidity. Cells were used at 80% confluence.

For viability test, cells were seeded in a 96-well plate at a density of 3×10^3 cells per well and cultured with normal medium for 24 h to allow attachment. Then, the medium was replaced by 100 μL extracts for each well. A Cell Counting Kit-8 (CCK-8, Dojindo Molecular Technology, Japan) was used to measure the cell viability and proliferation after 1, 2, and 4 days culture with gradiently diluted extracts. The culture medium was used as the negative control and medium with 10% DMSO (Invitrogen, USA) was used as the positive control.

For staining, cells were seeded on the sample surface at a density of 5×10^4 cells per sample and culture with 2 mL normal medium for 24 h before undergoing a Live/Dead staining procedure. Stained cells were observed using fluorescence microscopy (Olympus).

For ALP activity, cells were seeded in a six-well plate at 2×10^4 cells mL $^{-1}$ with 2 mL per well and cultured with normal medium to reach 80% confluence before replacing with an osteogenic extraction medium for 7 and 14 days. Culture medium was replaced every 48 h. The ALP activity was measured with ALP quantitative analysis kit (Nanjing Jiancheng Bioengineering Institute, China).

For osteogenic-related gene expression, a real-time PCR was used. During the same osteogenic culture procedure, cell differentiation was induced for 10 days. The total RNA was extracted using an Rneasy mini kit (Qiagen, Germany). β -actin was used as an internal reference to measure the mRNA expression of the marker genes (ALP, COL-1, OCN, and Runx-2) of cells using qt-PCR. The primer sequences are shown in **Table 2**. A

Table 2. Primer sequence of MC3T3-E1 cells.

Target gene	Direction	Primer sequence (5'-3')			
ALP	Forward	GGAGATGGTATGGGCGTCTC			
	Reverse	GGACCTGAGCGTTGGTGTTA			
Col I	Forward	TTCTCCTGGCAAAGACGGAC			
	Reverse	CTCAAGGTCACGGTCACGAA			
OCN	Forward	CTGACCTCACAGATCCCAAGC			
	Reverse	TGGTCTGATAGCTCGTCACAAG			
Runx-2	Forward	TCGGAGAGGTACCAGATGGG			
	Reverse	AGGTGAAACTCTTGCCTCGT			

reverse transcription kit (SuperScript III Reverse Transcriptase) was used to reverse 1 mg RNA. SYBR premix Ex Taq II ($2\times$) was used to perform qt-PCR in an ABI 7500 Fast machine (Applied Biosystems, Courtaboeuf, France).

Surgical Process: The detailed surgical procedure has been reported in our previous study. [5a] Here the implantation is described briefly. Implants are made of pure Zn and Zn-0.4Gd alloy pins (Φ 1.6 × 15 mm), which were machined from the as-extruded samples, and polished to 2000 grit surface condition. Pure Zn and Zn-0.4Gd alloy pins were sterilized by UV-radiation before surgery. A rat femur model was built by drilling a cylindrical hole (1.6 mm in diameter) in the center of the femoral condyle parallel to the long axis of the femur. Each group had six pins and each rat received one pin. All animals were sacrificed after 8 weeks and right femurs were explanted and fixed in formalin buffered solution followed by X-ray scan, Micro-CT, and histology. All animal operations and experiments were approved by the Animal Ethics Committee of Shanghai Rat & Mouse Biotech Co., Ltd (LL-20171120-01).

Micro-CT: Explanted rat femurs were observed by a Micro-CT system (Skyscan 1172, Bruker Micro-CT N. V., Belgium) with a 20 μm resolution protocol (100 kV, Al + Cu filter, 0.6° rotation step, 360° rotation). Three dimension reconstruction of the metallic implant and degradation products are based on their threshold difference using CT An software. Data analysis was conducted by Skyscan softwares.

Cross-Sectional Analysis: Explanted implants were embedded in epoxy resin and sliced into 1 mm thickness followed by grinding with 7000 grit paper and polished with diamond paste. The polished sample was further coated by gold before scanning by SEM equipped with EDS (Hitachi S-4800, Japan). Pitting corrosion analysis were carried out according to the ASTM G46-94. Pit size and depth were measured using ImageJ software. The size of the pit was defined as the portion of the implant perimeter that covers the pit. The depth of the pit is defined as the maximal length from the implant circumference to the bottom of the pit. At least three samples from different implants were used as parallel. Pit density was calculated by dividing the number of pits by the circumference of the implant. Method to obtain the penetration rate has been reported here. [32]

Histological Analysis: The explanted implants were fixed, rinsed in water, dehydrated in ethanol, cleared in xylene, and embedded in methyl methacrylate. Sections were created perpendicular to the long axis of implants followed by grinding to 100 µm thickness, polished and stained with van Gieson's Picrofuschin. Another group of samples was decalcified, embedded in paraffin, and sectioned before staining with Masson's trichrome and H&E. Then, stained samples were observed under a high-quality microscope (Olympus CKX41, Japan). Bone area (BA) was defined as a ratio of new bone area to total area extending 100 µm from the implant. Bone-to-implant contact (BIC) was the implant perimeter in contact with bone normalized over the implant perimeter.

Statistical Analysis: Data are expressed as mean \pm standard deviation ($n \ge 3$, independent samples). For normally distributed data sets with equal variances, one-way ANOVA testing followed by a Tukey post-hoc test was carried out across groups. In all cases, significance was defined



www.advancedsciencenews.com

www.advhealthmat.de

ADVANCED HEALTHCARE MATERIALS

as $p \leq 0.05$. Statistical analysis was carried out using OriginPro 2019b Software.

Acknowledgements

H.Y. and B.J. contributed equally to this work. This work was supported by the Natural Science Foundation of China (Grant No. 51931001, 5193000081, 5210010632) and the Fundamental Research Funds for the Central Universities (Grant No. JKF-YG-21-B003, YWF-22-T-105, YWF-22-L-1264).

Conflict of Interest

The authors declare no conflict of interest.

Data Availability Statement

The data that support the findings of this study are available from the corresponding author upon reasonable request.

Keywords

biodegradable materials, biodegradation, bone implants, bone regeneration, Zn-Gd alloys

Received: May 18, 2022 Revised: July 19, 2022 Published online:

- a) J. Ovesen, B. Møller-Madsen, J. Thomsen, G. Danscher, L. Mosekilde, *Bone* **2001**, *29*, 565; b) I. S. Kwun, Y. E. Cho, R. Lomeda, H. I. Shin, J. Y. Choi, Y. H. Kang, J. H. Beattie, *Bone* **2010**, *46*, 732.
- [2] a) L. Rossi, S. Migliaccio, A. Corsi, M. Marzia, P. Bianco, A. Teti, L. Gambelli, S. Cianfarani, F. Paoletti, F. Branca, J. Nutr. 2001, 131, 1142;
 b) M. Hie, N. Iitsuka, T. Otsuka, A. Nakanishi, I. Tsukamoto, Bone 2011, 49, 1152.
- [3] a) D. Liang, M. Yang, B. Guo, J. Cao, L. Yang, X. Guo, Biol. Trace Elem. Res. 2012, 146, 340; b) H. J. Seo, Y. E. Cho, T. Kim, H. I. Shin, I. S. Kwun, Nutr. Res. Pract. 2010, 4, 356.
- [4] a) M. Hie, I. Tsukamoto, Eur. J. Pharmacol. 2011, 668, 140; b) M. Yamaguchi, M. N. Weitzmann, Mol. Cell. Biochem. 2011, 355, 179.
- [5] a) H. Yang, B. Jia, Z. Zhang, X. Qu, G. Li, W. Lin, D. Zhu, K. Dai, Y. Zheng, Nat. Comm. 2020, 11, 401; b) H. Yang, X. Qu, M. Wang, H. Cheng, B. Jia, J. Nie, K. Dai, Y. Zheng, Chem. Eng. J. 2021, 417, 129317; c) X. Qu, H. Yang, B. Jia, Z. Yu, Y. Zheng, K. Dai, Acta Biomater. 2020, 117, 400; d) B. Jia, H. Yang, Y. Han, Z. Zhang, X. Qu, Y. Zhuang, Q. Wu, Y. Zheng, K. Dai, Acta Biomater. 2020, 108, 358; e) H. Yang, X. Qu, W. Lin, D. Chen, D. Zhu, K. Dai, Y. Zheng, ACS Biomater. Sci. Eng. 2019, 5, 453; f) H. Yang, X. Qu, W. Lin, C. Wang, D. Zhu, K. Dai, Y. Zheng, Acta Biomater. 2018, 71, 200; g) H. F. Li, X. H. Xie, Y. F. Zheng, Y. Cong, F. Y. Zhou, K. J. Qiu, X. Wang, S. H. Chen, L. Huang, L. Tian, L. Qin, Sci. Rep. 2015, 5, 10719; h) Z. Zhang, B. Jia, H. Yang, Y. Han, Q. Wu, K. Dai, Y. Zheng, Bioact. Mater. 2021, 6, 3999.
- [6] H. Guo, D. Xia, Y. Zheng, Y. Zhu, Y. Liu, Y. Zhou, Acta Biomater. 2020, 106, 396.

- [7] Y. Zhuang, Q. Liu, G. Jia, H. Li, G. Yuan, H. Yu, ACS Biomater. Sci. Eng. 2020, 7, 893.
- [8] a) D. Zhu, Y. Su, M. L. Young, J. Ma, Y. Zheng, L. Tang, ACS Appl. Mater. Interfaces 2017, 9, 27453; b) N. Murni, M. Dambatta, S. Yeap, G. Froemming, H. Hermawan, Mater. Sci. Eng., C 2015, 49, 560; c) J. P. O'Connor, D. Kanjilal, M. Teitelbaum, S. S. Lin, J. A. Cottrell, Materials 2020, 13, 2211.
- [9] Y. Su, K. Wang, J. Gao, Y. Yang, Y.-X. Qin, Y. Zheng, D. Zhu, Acta Biomater. 2019, 98, 174.
- [10] G. K. Levy, A. Kafri, Y. Ventura, A. Leon, R. Vago, J. Goldman, E. Aghion, *Mater. Lett.* 2019, 248, 130.
- [11] E. Jablonská, D. Vojtěch, M. Fousová, J. Kubásek, J. Lipov, J. Fojt, T. Ruml, Mater. Sci. Eng., C 2016, 68, 198.
- [12] a) H. Kabir, K. Munir, C. Wen, Y. Li, Bioact. Mater. 2021, 6, 836; b) G. Katarivas Levy, J. Goldman, E. Aghion, Metals 2017, 7, 402.
- [13] a) H. Li, H. Yang, Y. Zheng, F. Zhou, K. Qiu, X. Wang, Mater. Des. 2015, 83, 95; b) B. Jia, H. Yang, Z. Zhang, X. Qu, X. Jia, Q. Wu, Y. Han, Y. Zheng, K. Dai, Bioact. Mater. 2021, 6, 1588.
- [14] a) J. Liu, D. Bian, Y. Zheng, X. Chu, Y. Lin, M. Wang, Z. Lin, M. Li, Y. Zhang, S. Guan, *Acta Biomater.* 2020, 102, 508; b) E. Willbold, X. Gu, D. Albert, K. Kalla, K. Bobe, M. Brauneis, C. Janning, J. Nellesen, W. Czayka, W. Tillmann, *Acta Biomater.* 2015, 11, 554.
- [15] a) H. Waizy, J. Diekmann, A. Weizbauer, J. Reifenrath, I. Bartsch, V. Neubert, R. Schavan, H. Windhagen, J. Biomater. Appl. 2014, 28, 667; b) C. Di Mario, H. Griffiths, O. Goktekin, N. Peeters, J. Verbist, M. Bosiers, K. Deloose, B. Heublein, R. Rohde, V. Kasese, J. Interv. Cardiol. 2004, 17, 391.
- [16] a) D. Bian, J. Deng, N. Li, X. Chu, Y. Liu, W. Li, H. Cai, P. Xiu, Y. Zhang, Z. Guan, ACS Appl. Mater. Interfaces 2018, 10, 4394; b) W. Liu, F. Cao, L. Chang, Z. Zhang, J. Zhang, Corro. Sci. 2009, 51, 1334; c) J. F. Nie, Y. Zhu, J. Liu, X. Y. Fang, Science 2013, 340, 957.
- [17] T. Haley, K. Raymond, N. Komesu, H. Upham, Br. J. Pharmacol. Chemother. 1961, 17, 526.
- [18] A. Myrissa, S. Braeuer, E. Martinelli, R. Willumeit-Römer, W. Goessler, A. M. Weinberg, Acta Biomater. 2017, 48, 521.
- [19] P. Forsyth, R. King, G. Metcalfe, B. Chalmers, *Nature* **1946**, *158*, 875
- [20] K. S. Jyotheender, M. P. Kumar, C. Srivastava, Appl. Surf. Sci. 2021, 559, 149953.
- [21] S. Thomas, N. Birbilis, M. S. Venkatraman, I. S. Cole, Circ. Res. 2012, 68, 160.
- [22] a) H. Yang, C. Wang, C. Liu, H. Chen, Y. Wu, J. Han, Z. Jia, W. Lin, D. Zhang, W. Li, *Biomaterials* 2017, 92, 145; b) P. K. Bowen, J. Drelich, J. Goldman, Adv. Mater. 2013, 25, 2577.
- [23] A. Cerovic, I. Miletic, S. Sobajic, D. Blagojevic, M. Radusinovic, A. E. Sohemy, Biol. Trace Elem. Res. 2007, 116, 61.
- [24] D. Chen, L. Waite, W. Pierce, Biol. Trace Elem. Res. 1999, 68, 225.
- [25] M. Nagata, B. Lönnerdal, J. Nutr. Biochem. 2011, 22, 172.
- [26] P. Marie, Bone 2006, 38, 10.
- [27] D. W. Bruce, B. E. Hietbrink, K. P. DuBois, *Toxicol. Appl. Pharmacol.* 1963, 5, 750.
- [28] E. A. Takahashi, D. F. Kallmes, K. C. Mara, W. S. Harmsen, S. Misra, Diagn. Interv. Radiol. 2018, 24, 378.
- [29] T. Grobner, F. Prischl, Kidney Int. 2007, 72, 260.
- [30] X. Tong, L. Zhu, K. Wang, Z. Shi, S. Huang, Y. Li, J. Ma, C. Wen, J. Lin, Acta Biomater. 2022, 142, 361.
- [31] a) Y. Li, Q. Pan, J. Xu, X. He, H. A. Li, D. A. Oldridge, G. Li, L. Qin, J. Orthop. Trans. 2021, 27, 110; b) K. Xie, L. Wang, Y. Guo, S. Zhao, Y. Yang, D. Dong, W. Ding, K. Dai, W. Gong, G. Yuan, J. Orthop. Trans. 2021, 27, 96.
- [32] P. K. Bowen, A. Drelich, J. Drelich, J. Goldman, J. Biomed. Mater. Res., Part A 2015, 103, 341.